Assessing post-fire ground cover in Mediterranean shrublands with field spectrometry and digital photography

Raquel Montorio Llovería [a,c,*], Fernando Pérez-Cabello [a,c], Alberto García-Martín [b,c]

[a] Department of Geography and Spatial Management, University of Zaragoza, C/ Pedro Cerbuna 12, 50009 Zaragoza, Spain
[b] Centro Universitario de la Defensa de Zaragoza, Academia General Militar, Ctra. Huesca s/n, 50090 Zaragoza, Spain
[c] Environmental Sciences Institute (IUCA), University of Zaragoza, C/ Pedro Cerbuna 12, 50009 Zaragoza, Spain

A B S T R A C T

Fire severity can be assessed by identifying and quantifying the fractional abundance of post-fire ground cover types, an approach with great capacity to predict ecosystem response. Focused on shrubland formations of Mediterranean-type ecosystems, three burned areas (Ibieca and Zuera wildfires and Peñaflor experimental fire) were sampled in the summers of 2006 and 2007. Two different ground measurements were made for each of the 356 plots: (i) 3-band high spatial resolution photography (HSRP) and (ii) the hemispherical-conical reflectance factor (HCRF) in the visible to near-infrared spectral range (VNIR, 400–900 nm). Stepwise multiple lineal regression (SMLR) models were fitted to spectral variables (HCRF, first derivative spectra or FDS, and four absorption indices) to estimate the fractional cover of seven post-fire ground cover types (vegetation and soil – unburned and charred components – and ash – char and ash, individually and as a combined category). Models were developed and validated at the Peñaflor site (training, $n = 217$; validation, $n = 88$) and applied to the samples from the Ibieca and Zuera sites ($n = 51$). The best results were observed for the abundance estimations of green vegetation ($R^2_{adj.}$ 0.70–0.90), unburned soil ($R^2_{adj.}$ 0.40–0.75), and the combination of ashes ($R^2_{adj.}$ 0.65–0.80). In comparison of spectral data, FDS outperforms reflectance or absorption data because of its higher accuracy levels and, importantly, its greater capacity to yield generalizable models. Future efforts should be made to improve the estimation of intermediate severity levels and upscaling the developed models. In the context of fire severity assessment, our study demonstrates the potential of hyperspectral data to estimate in a quick and objective manner post-fire ground cover fractions and thus provide valuable information to guide management responses.

© 2016 International Society for Photogrammetry and Remote Sensing, Inc. (ISPRS). Published by Elsevier B.V. All rights reserved.

1. Introduction

Immediate or first-order effects of fire on an environment, referred to as fire severity following the terminology of Lentile et al. (2006), Veraverbeke et al. (2010) and others, is of interest to forest management primarily because it is presumed to be an indicator of long-term ecosystem response (also referred to as burn severity or second-order effects). Many researchers have already shown its influence on vegetation recovery (Díaz-Delgado et al., 2003), changes in below-ground flora and fauna (Neary et al., 1999), seedling germination after fire (De Luís et al., 2005), species richness (Keeley et al., 2005), changes in soil structure (Mataix-Solera and Doerr, 2004), and runoff and erosion processes (Doerr et al., 2006; Moody et al., 2013), among others.

An adequate remote sensing assessment of fire severity is of great importance, especially in a region such as the Mediterranean, where forest fire size and frequency are increasing (Tedim et al., 2013) and higher intensity and severity levels are being observed (Chuvieco et al., 2008). Traditional assessment has been based on spectral indices derived from multispectral satellite imagery, mostly from Landsat TM or ETM+ sensors (a.o. Epting et al., 2005; Picotte and Robertson, 2011; van Wagtendonk et al., 2004). The normalized ratio of near-infrared (NIR, band 4) and short-wave infrared (SWIR, band 7), known as the Normalized Burn Ratio (NBR, López and Caselles, 1991), and its delta or relative delta versions (dNBR and RdNBR, Key and Benson, 2006; Miller and Thode, 2007) have been widely applied empirically to estimate the field severity index Composite Burn Index (CBI, Key and Benson,

* Corresponding author at: Department of Geography and Spatial Management, University of Zaragoza, C/ Pedro Cerbuna 12, 50009 Zaragoza, Spain. Tel.: +34 876 55 38 51.

E-mail addresses: montorio@unizar.es (R. Montorio Llovería), fcabello@unizar.es (F. Pérez-Cabello), algarcia@unizar.es (A. García-Martín).

2006) or its modified version, the GeoCBI (De Santis and Chuvieco, 2009). Although moderate to high determination coefficients are frequently observed (a.o. Tanase et al., 2011; Veraverbeke et al., 2010), a number of limitations and disadvantages of this approach have been reported in the literature (see Lentile et al., 2009 for examining the limitations in detail). Apart from the criticism of the performance of NBR as a severity index (Roy et al., 2006), the arguments against a CBI that mixes first and second-order effects (Keeley, 2009), or the uncertainties regarding the best suitability of NBR from a mono- or bi-temporal point of view, and between initial or extended assessment (e.g. Epting et al., 2005; Hudak et al., 2007; Picotte and Robertson, 2011; Veraverbeke et al., 2010; Zhu et al., 2006), two main drawbacks of this approach can be highlighted. These are: (i) some studies developed in Mediterranean areas report an inadequate prediction of second order effects in terms of vegetal regeneration (Keeley et al., 2008; Vicente-Serrano et al., 2011) and erosion (Pérez-Cabello et al., 2006); and (ii) spectral indices are physically meaningless without field calibration (Hudak et al., 2007; Lentile et al., 2006).

Identification and quantification of the fractional abundance of post-fire ground cover types has emerged as an alternative approach for fire severity assessment (Lentile et al., 2006; Roy et al., 2013). A typical post-fire environment is thus considered to be a mixture of vegetation and soil, as unburned cover types, with ash and charred components (a.o. Edwards et al., 2013; Lewis et al., 2007; Robichaud et al., 2007; Veraverbeke et al., 2012b). In contrast to the spectral indexes, as Lentile et al., 2009 points out, this approach produces measures with a physical meaning, directly analogous to traditional field measurements of % green, % brown, and % black. Furthermore, many researchers have shown the important influence of these cover types on ecosystem response: e.g., presence of green vegetation controls runoff and erosion processes (Cerdà and Doerr, 2005); charred vegetation increases soil water retention and decreases overland flow and soil losses (Cerdà and Doerr, 2008; Pannkuk and Robichaud, 2003; Shakesby and Doerr, 2006); loss of organic matter in burned soils alters aggregate stability and porosity and then resistance to erosion and infiltration rates (Arcenegui et al., 2008; Doerr et al., 2006; Mataix-Solera and Doerr, 2004; Mataix-Solera et al., 2002); presence of an ash layer may reinforce or delay overland flow (Balfour et al., 2014; Bodí et al., 2012; Cerdà and Doerr, 2008), can increase or decrease sediment concentration depending on the temporal approach (Cerdà and Doerr, 2008; Pérez-Cabello et al., 2012; Woods and Balfour, 2008), and can alter soil hydrophobicity depending on the soil and ash properties and the ash thickness (Bodí et al., 2011).

Using different techniques such as sub-pixel methods (SMA, a.o. Lewis et al., 2011; Veraverbeke et al., 2012b and MTFM, a.o. Lewis et al., 2008; Robichaud et al., 2007) or continuum-removal transformation (Kokaly et al., 2007), hyperspectral data have been the basis of studies developed under this approach. Hyperspectral sensors provide data in contiguous narrow bands of reflectance spectra, thus offering a greater capability to distinguish specific spectral features and thereby identify the diversity of post-fire cover types. Visible to short-wave infrared (VSWIR, 0.4–2.5 μm) has been the spectral range most deeply explored, although recent research has also examined the potential benefits of a combination of VSWIR and mid to thermal infrared (MTIR, 3.5–12.5 μm) data (Veraverbeke et al., 2012a).

In this context, we aim to explore and characterize the spectral properties of post-fire ground cover types and develop empirical models that allow the quantification of their fractional abundance. We focus on Mediterranean shrubland areas and work with field methodologies (high spatial resolution photography and field spectrometry) that provide an accurate mapping of observed fractions and hyperspectral reflectance values. Using original and transformed spectral data, we assess the accuracy of the models and the suitability of the spectral datasets in a practical application of the results.

2. Study area

In a broader sense, this study focuses on the shrubland formations of Mediterranean areas. Various reasons explain the interest in these formations. Shrublands are one of the most important plant formations in Mediterranean-type ecosystems. Considering its dynamic, shrublands now occupy abandoned arable fields (Gartzia et al., 2014; Lasanta et al., 2011) and are also replacing previously forested areas as a consequence of increasing fire frequency and severity (De Luís et al., 2006; Pausas et al., 2008). Following this growing trend, they constitute the highest percentage of annual burned area in Spain over the last decade (data from the Spanish Statistical Office http://www.ine.es/dyngs/IOE/es/operacion.htm?numinv=04002, accessed October 10, 2015). This highlights their interest from a forest fire perspective, especially as future climatic trends will tend to reinforce the changes already observed (Komac et al., 2013; Rodrigo et al., 2004), pointing to higher fire risk indices in these shrub-type species Mouillot et al., 2002. From a fire severity viewpoint, shrubland is the vegetation type where assessment of this variable has achieved less satisfactory results (Epting et al., 2005), and consequently where the hyperspectral approach could produce the most significant progress (Finley and Glenn, 2010). Finally, the low height of this plant formation provides the perfect methodological setting to apply the selected field techniques.

Specifically, post-fire ground cover in Mediterranean shrublands was examined in three burned areas in Aragón, in the northeast of the Iberian Peninsula (Fig. 1). Shrubland formations in these areas vary according to location, from the semiarid environment in the central Ebro Depression to the transitional environment of the Pyrenees.

The first area is the wildfire that occurred in Ibieca (I_{WF}) on June 14th, 2006, where 300 ha of crops and 200 ha of shrubland and *Quercus ilex* L. were burned. The specific study site (coordinates of centroid X, Y: 732,345E, 4,671,170N, UTM 30T, European Datum 1950; EPSG 23030) covers 3200 m² and is composed of *Juniperus oxycedrus* L., *Rubia peregrina* L., and *Ligustrum vulgare* L. as main plant species.

The second area is also a wildfire, occurring in the pine forest of Zuera (Z_{WF}) on July 25th, 2006. Caused by lighting, the fire burned 40 ha of *Pinus halepensis* Mill. and a dense shrub understory of *Quercus coccifera* L., *Rosmarinus officinalis* L., *Thymus vulgaris* L., *Genista scorpius* L., and *Juniperus communis* Lam. at the study site (coordinates of centroid X, Y: 671,501E, 4,639,210N, UTM 30T, European Datum 1950; EPSG 23030).

The third area is in Peñaflor (P_{EF}) where two experimental fire plots, covering a total area of 455 m², were burned on October 19th, 2007 (coordinates of centroid X, Y: 685,539E, 4,628,820N, UTM 30T, European Datum 1950; EPSG 23030). The experimental fire plots consisted of sparse shrubland dominated by *Rosmarinus officinalis* L. and *Brachypodium retusum* Pers. The species *Helianthemum lavandulifolium* Desf., *Helianthemum marifolium* L., *Thymus vulgaris* L., *Artemisia herba-alba* Asso., *Salsola vermiculata* L., and *Linum strictum* L. were also present.

3. Materials and methods

3.1. Ground measurements

3.1.1. Experimental design

Data were acquired in the immediate hours or days after the fire events, giving a total sample of 356 plots from the three study sites
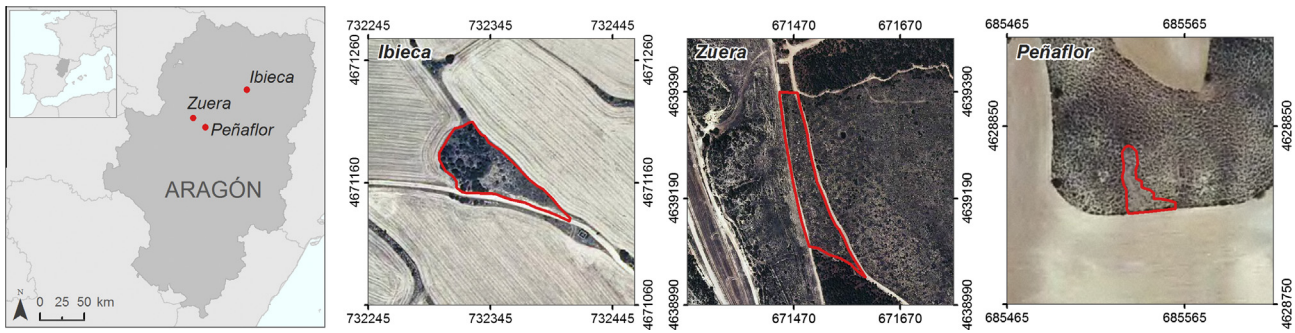
Fig. 1. Location map and aerial views of the study sites: wildfires at Ibieca (I_{WF}) and Zuera (Z_{WF}) and the experimental fire at Peñaflor (P_{EF}).

(Table 1). Considering the errors in spectral measures related to illumination conditions (Milton et al., 2009), field measurements were made on days with clear weather conditions, with direct solar irradiance being the dominant source of energy incident on the target (Table 2). In the same way, measurements were restricted to a 2-h period around solar noon, when changes in the solar zenith angle are lower.

Field techniques – high spatial resolution photography or HSRP (adapted from the original methodology detailed in Pérez-Cabello et al. (2012)), and field spectrometry – were applied sequentially in each plot. Platforms were used to maintain a fixed viewing geometry between the sensor and the target (constant height, nadir position) and to ensure both sensors (digital camera and field spectroradiometer) were sensing the same area (Fig. 2). Two different platforms were used depending on the sampling pattern selected (Table 1). In the Ibieca and Zuera study sites, with a greater surface area, a simple random sampling pattern with a mobile platform (height 1.5 m, width 0.7 m, Fig. 2 above) was applied. The number of plots sampled in these sites ($n = 14$ and $n = 37$ in I_{WF} and Z_{WF} sites, respectively) was influenced by the need to cover a big surface in a restricted time period, and using a platform with only one measuring point, which involved the installation and removal of both sensors at each plot and also the individual calibration of each spectral measurement.

At the Peñaflor experimental fire site, a larger platform (height 2 m, width 3 m, Fig. 2 below) was used. This platform allowed the application of a systematic sampling pattern of 35 points (resulting from the combination of seven marked positions placed 40-cm apart in the longitudinal axis and five anchor points placed 50-cm apart in the mobile superior crossbar, see red marks in Fig. 2 below). New sampling strategy was significantly less time-consuming because the installation of sensors and the spectral calibration was made only once for each platform location, a total of ten positions spatially distributed in the study site and covering unburned and burned ground covers. Therefore, a higher number of samples ($n = 305$, after the removal of erroneous data) were obtained in a relatively small burned area.

3.1.2. High spatial resolution photographs

Vertical high spatial resolution photographs (HSRP) were obtained with a digital camera Reflex Nikon D70 in the visible

(VIS) spectral range with a 0.5-mm spatial resolution (Pérez-Cabello et al., 2012). Remote control of the digital camera, attached to the platforms described above, allowed the operators to remain some distance from the target during measurements and thus avoid shadow problems.

3.1.3. Field spectrometer data

Measurements of the hemispherical conical reflectance factor (HCRF) (Schaepman-Strub et al., 2006) were captured using two field spectroradiometers, both over the 400–900 nm wavelength range (visible, VIS, to near infrared regions, NIR) but with differences in their spectral characteristics. The Ocean Optics USB2000, used for the wildfire sites of Ibieca and Zuera, reports reflectance for 1462 channels at a 0.33-nm sampling interval, 1.34-nm FWHM (full width half maximum) spectral resolution, and a signal-to-noise ratio (SNR) of 250:1. The Avantes AvaSpec-2048, used for the Peñaflor experimental fire site, reports reflectance for 874 channels at a 0.57-nm sampling interval, 2.4-nm FWHM spectral resolution, and SNR of 200:1. Both field spectroradiometers were calibrated against a Spectralon (Labsphere Inc., North Sutton, NH, USA) ~100% reflective panel at frequent intervals during field spectra collection. Every spectrum was corrected for dark current effect and was obtained from an average of 20 spectra to avoid random noise in sample and calibration panel measurements. Spectra from the Ocean Optics instrument were collected with a 10° foreoptic from a height of ~1.5 m (Field of view (FOV) 13-cm radius). Spectra from the Avantes AvaSpec instrument were collected with a bare tip foreoptic (25°) from a height of ~2 m (FOV 44-cm radius). Both FOV were assumed to be homogenous (Table 1 and Fig. 2).

Two different tests were applied to assess the quality of spectral data regarding (1) wavelength shift and (2) intercomparison of reflectance values. (1) In the wavelength test, calibrated light sources (blue, green, red, and NIR LED lamps) were used as reference. Low root mean square error (RMSE) values (~1 nm and ~2.5 nm) were observed in both sensors for VIS and NIR regions, respectively, always with a negative bias. (2) In the reflectance values test, spectra measured with the two sensors were compared. The same surface of a photosynthetically active leaf was captured by both sensors and under the same controlled illumination conditions. Very low error values (RMSE ~ 0.3% and ~0.5% for the VIS and NIR regions, respectively) were also observed, with a slight

Table 1
Experimental design data.

Study site	Fire date (dd/mm/yy)	Fieldwork date	Number of plots	Field spectroradiometer	Platform	Sampling	FOV radius
I_{WF}	14/06/06	26/06/06	14	Ocean Optics USB 2000	1.5 m height	Random	13 cm
Z_{WF}	25/07/06	28/07/06	37	Ocean Optics USB 2000	1.5 m height	Random	13 cm
P_{EF}	19/10/07	19/10/07	305	Avantes AvaSpec-2048	2 m height	Systematic	44 cm

Table 2
Illumination conditions of fieldwork days.

Study site	Fieldwork date	Weather conditions				Illumination geometry	
		Average air temperature (°C)	Precipitation (mm)	Direct solar radiation (w/m²)	Diffuse solar radiation (w/m²)	Solar time (GTM+00)	Change in solar zenith angle
I$_{WF}$	26/06/06	28.7	0	3212	556	10:52–12:30	4°
Z$_{WF}$	28/07/06	27.1	0	3028	550	10:47–11:43	3°
P$_{EF}$	19/10/07	18.6	0	2604	291	10:33–13:06	5°

*Solar radiation data were provided by the Spanish meteorological agency (AEMET).
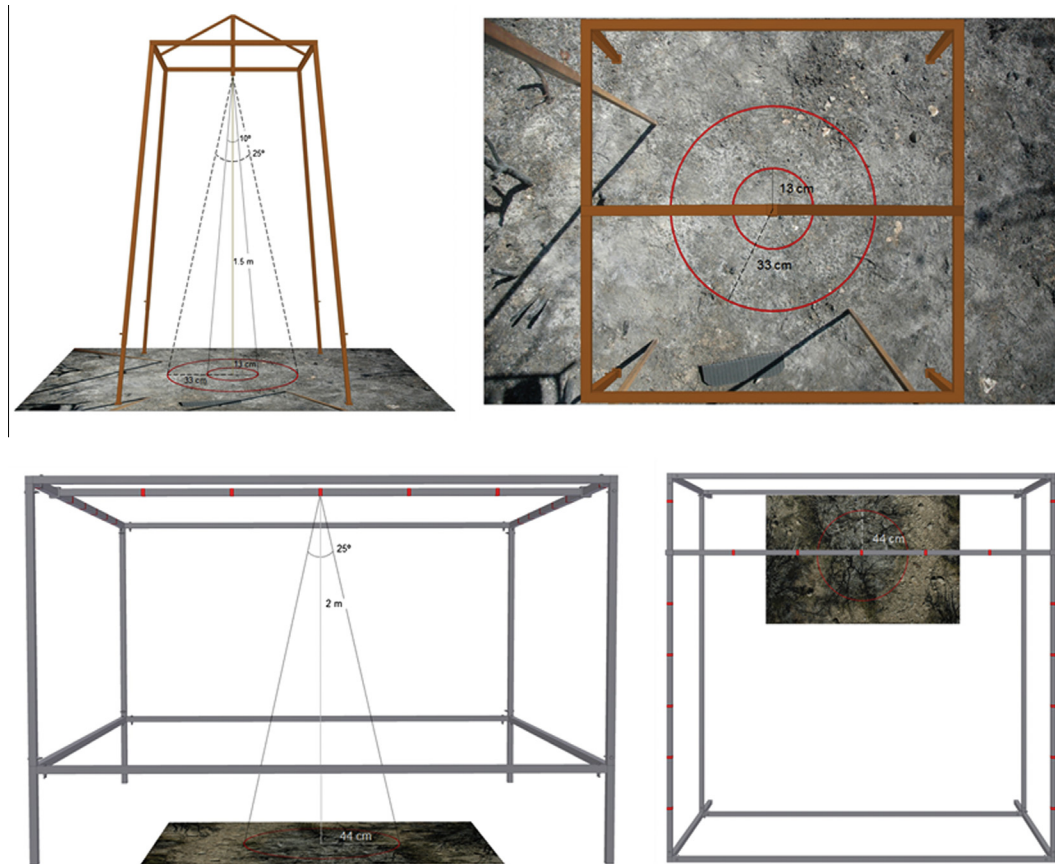
Fig. 2. Viewing geometry: front and top view of the sampling platforms. Photographs show a detail of various FOVs at the target depending on the instrument's field of view and sensor-target distance.

overestimation of values (bias ~ 0.1%) in the VIS region of the Avantes AvaSpec spectroradiometer compared to the Ocean Optics, and vice versa in the NIR region (bias ~ −0.5%).

3.2. Data processing

3.2.1. HSRP-derived estimates of post-fire ground cover components

The area sensed by the field spectroradiometers (13-cm or 44-cm radius from the nadir position) was extracted from the digital photographs obtained by HSRP. The 356 circular-shaped files were merged in mosaic images (one image per study site) to apply a supervised classification process in a homogeneous and simultaneous manner. According to HSRP procedure (Pérez-Cabello et al., 2012), the method involved a three-spectral supervised maximum likelihood classification. After establishing the training areas using photo-interpretation, the mean values and variances of the digital numbers (DNs) for the three bands used in classification were calculated from all the pixels in each class. The classification works by comparing every pixel of the HSRP images with the various

signatures obtained in the training process, and assigning them to the class with the closest signature.

The fractional cover of six post-fire ground cover components was estimated as a result of the classification process: green unburned vegetation (GV), unburned soil (UBS), brown non-photosynthetic vegetation (NPV) or scorched vegetation, burned soil (BS), black char, and white ash (Fig. 3a). The shadow component was also estimated so that all cover fractions summed to unity.

Classification accuracy was evaluated from a validation sample of n = 210 (70 random points in each of the 3 burned areas). Global accuracy of the classification map obtained is 93%, with a Cohen's Kappa coefficient of 0.83 (Table 3). As observed in the confusion matrix, GV is the ground cover with the highest classification accuracy (user's and producer's accuracy of 100%) and, conversely, BS throws the lowest value (user's and producer's accuracy of 38% and 33%, respectively), with problems with the remaining categories except GV. Accuracy values of UBS, NPV, char, ash, and shadow range from 0.82 to 0.96, observing some confusion
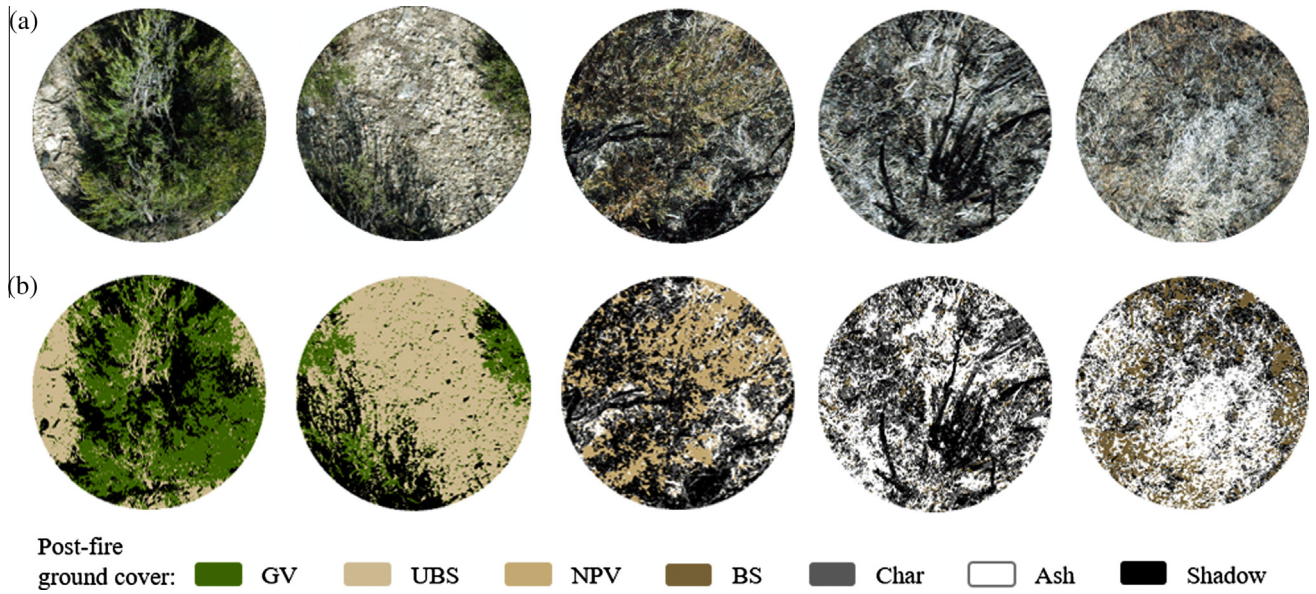
Fig. 3. Estimation of post-fire ground cover components: (a) original photographs and (b) detail of the classification results obtained.

between char/ash and char/shadow pairs. Fig. 3b shows examples of the accuracy achieved in discrimination of the surface cover.

3.2.2. Processing of surface spectral reflectance data

Three different processes were applied to the spectral database in order to improve the signal-to-noise ratio (SNR) and obtain new hyperspectral variables.

A Savitzky–Golay filter was used to smooth the spectral data in the 400–900 nm spectral region (Savitzky and Golay, 1964; Steinier et al., 1972). According to the depth of the absorption features and the FWHM of the data, a polynomial degree 3 and a filtersize 40 (27-nm and 46-nm width of the smoothing window in the data from the Ocean Optics and Avantes AvaSpec instruments, respectively) were the parameters chosen, improving the SNR by a factor of 9.

Derivative transformation and spectral feature analysis methods were applied to the smoothed spectra to calculate the slope values from the reflectance and to identify and isolate absorption features. Standard first derivative reflectance spectra (FDS) and normalized reflectance with the continuum removal method (R') were the new hyperspectral variables obtained (Eqs. (1) and (2)). Four absorption indices were also calculated from the continuum-removed reflectance spectra (Eqs. (3)–(6)): band depth (BD), band depth ratio or band depth normalized to

band depth at the center (BDR), normalized band depth index (NBDI), and band depth normalized to area (BNA).

$$FDS_{\lambda(x)} = \frac{R_{\lambda(y)} - R_{\lambda(x)}}{\lambda_{(y)} - \lambda_{(x)}} \tag{1}$$

where $FDS_{\lambda(x)}$ is the first derivative reflectance spectra in the waveband x, and $R_{\lambda(x)}R_{\lambda(y)}$ are the reflectance values of the consecutive wavebands x and y (Dawson and Curran, 1998).

$$R'_{(\lambda i)} = \frac{R_{(\lambda i)}}{Rc_{(\lambda i)}} \tag{2}$$

where $R'_{(\lambda i)}$ is the continuum-removed reflectance, $R_{(\lambda i)}$ is the reflectance value for each waveband in the absorption feature, and $Rc_{(\lambda i)}$ is the reflectance level of the continuum line (convex hull) at the corresponding wavelength (Mutanga et al., 2004).

$$BD_{(\lambda i)} = 1 - R'_{(\lambda i)} \tag{3}$$

$$BDR_{(\lambda i)} = \frac{BD_{(\lambda i)}}{D_c} \tag{4}$$

$$NBDI_{(\lambda i)} = \frac{BD_{(\lambda i)} - D_c}{BD_{(\lambda i)} + D_c} \tag{5}$$

Table 3
Confusion matrix of the classification map derived from HSRP.

Ground truth	Classification								Producer's accuracy
	GV	UBS	NPV	BS	Char	Ash	Shadow	Total	
GV	22	0	0	0	0	0	0	22	1.00
UBS	0	38	0	5	0	1	0	44	0.86
NPV	0	0	18	4	0	0	0	22	0.82
BS	0	3	2	6	3	4	0	18	0.33
Char	0	0	0	0	36	2	0	38	0.95
Ash	0	0	0	1	3	42	0	46	0.91
Shadow	0	0	0	0	2	0	18	20	0.90
Total	22	41	20	16	44	49	18	210	
User's accuracy	1.00	0.93	0.90	0.38	0.82	0.86	1.00		

Overall accuracy: 0.93
  Cohen's Kappa: 0.83

$$BNA_{(\lambda i)} = \frac{BD_{(\lambda i)}}{A} \qquad (6)$$

where $R'_{(\lambda i)}$ is the continuum-removed reflectance at waveband i; $BD_{(\lambda i)}$ is the band depth at waveband i; D_c is the band center, which is the maximum band depth; and A is the area of the absorption feature (Curran et al., 2001; Mutanga et al., 2004).

3.3. Statistical analysis

Stepwise multiple lineal regression (SMLR) models were fitted to independent explanatory variables – that is, the six spectral datasets (HCRF, FDS, BD, BDR, NBDI, BNA) – to estimate the dependent variables – that is, fractional cover estimation of six individual post-fire ground cover components (GV, UBS, NPV, BS, char and ash) and a mixed category obtained by combining the last two ash-related covers. HCRF and FDS equations were generated from the entire spectrum (874 wavebands from 400 to 900 nm), whereas 66% of each spectrum (574 wavebands of the two absorption features described in Section 4.1) was used in the absorption datasets. The primary assumptions of regression analysis were tested and satisfied: (i) linearity, by visual analysis of residual plots showing the standardized residuals vs. the predicted values; (ii) independence of errors, by Durbin–Watson statistic; (iii) normality, through histograms of the standardized residuals; (iv) collinearity, through tolerance, variance inflation factors (VIF) and condition index; and (iv) homocedasticity, by visual examination of a plot of the standardized residuals vs. the standardized predicted values.

The stepwise regression was run separately for each of the previous combinations for a total of 42 runs. Their prediction power was compared using the association strength between variables, which was expressed by the adjusted determination coefficient ($R^2_{adj.}$) and the amount of error, which was expressed by the root mean square error (RMSE).

A total of 217 plots at the P_{EF} site ($n = 305$) were randomly selected as a training set using a ratio of 70–30. The full range of post-fire components (severity levels) was represented in this subsample. The remaining 88 points at the P_{EF} site and 51 points at the I_{WF} and Z_{WF} sites (IZ_{WF}) were used as two validation sets. Specifi-

cally, the validation in IZ_{WF} dataset can be considered an evaluation of the potential to apply the empirical models in natural fires and to different sensors. The empirical fitting was evaluated using the $R^2_{adj.}$ and RMSE between observed and predicted values.

Comparison of endmembers between the three burned areas was made using the mean absolute error (MAE).

4. Results

4.1. Spectral properties of post-fire ground cover components

The spectrum average of non-mixed samples of each post-fire ground cover (abundance values higher than 75%) was used as endmember for spectral characterization. The spectral curves of the endmembers in reflectance, FDS, and BD values are presented graphically in Fig. 4. Specific data on the absorption features observed in GV endmembers are also included in Table 4.

The spectral signatures observed in the three study sites are in line with what has been reported in the literature. GV shows the well-documented contrast between the VIS and the NIR regions (low and high reflectance values, respectively), with two absorption features associated with leaf pigments and centered around 500 nm and 680 nm (Fig. 4 and Table 4). Continua endpoints of the absorption features observed are within ±15 nm of the limits described in other publications (Curran et al., 2001; Kokaly et al., 2003; Noomen et al., 2006). The FDS of GV clearly shows the greater amount of spectral variation in this ground cover. Fire results in the removal of absorption features and the loss of spectral variation. Thus, NPV exhibits higher reflectance values in the VIS region and lower values in the NIR region, and consequently a flatter derivative spectral profile. The 680-nm absorption feature is still visible in the NPV ground cover but with a great loss of absorption depth and width (mean band depth from 0.75 to 0.19 and mean band width from 120 nm to 40 nm).

UBS reflectance increases linearly by around 15–30% over the 400–900 nm spectral range and is spectrally featureless in terms of notable absorption features. BS exhibits a similar spectral reflectance pattern to UBS but with lower reflectance values (decreases of ~5% in the 400 nm and ~15% in the 900 nm).
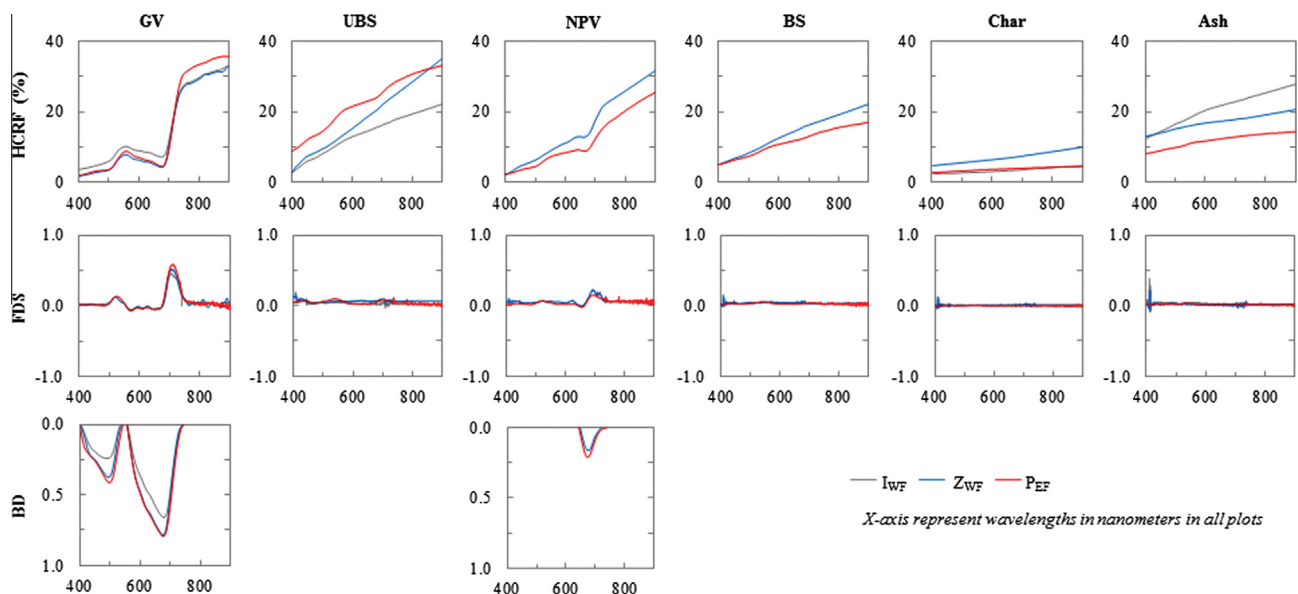
Fig. 4. Mean spectral signatures of post-fire ground cover components (GV, UBS, NPV, BS, char and ash) collected from the study sites. Spectral curves are for HCRF reflectance (above), first derivative spectra (middle), and band depth (below). See Table 4 for further details on the 500-nm and 680-nm absorption features.

Table 4
Continuum endpoints and band center definitions for the 500-nm and 680-nm absorption features observed in the reflectance spectra of GV endmembers in the three study sites.

Study site	Designation of absorption feature	Location of absorption feature		
		Short wavelength end	Band Center	Long wavelength end
I_{WF}	500	400.25	492.79	533.64
	680	557.26	680.01	749.21
Z_{WF}	500	400.25	494.98	539.39
	680	556.90	678.31	746.23
P_{EF}	500	400.24	498.25	543.69
	680	558.20	678.56	745.73

Note: All wavelengths are given in nm.

Char has a very low spectral reflectance right across the 400–900 nm spectral range (<10%) and is spectrally featureless. According to other authors (Smith et al., 2005), its presence in the burned areas represents the point with the lowest mean and variance of the surface spectral reflectance at all wavelengths. Ash exhibits a significantly higher reflectance than char, with values that increase from VIS to NIR at a higher rate (<5% in char and ∼5–15% in ash).

Comparison of the study sites shows differences between the spectral curves of the endmembers. Mean absolute error values reveal that the greatest contrast is in the HCRF comparison (MAE values in the range 0.33–9.25% and a mean global value of 4% for the three burned areas), especially in the UBS and ash covers (MAE values higher than 6%), and that FDS transformation softens the differences and even the spectral behavior of the post-fire ground cover between the burned areas (MAE values in the range 0.5–2.8% with a mean global value of 1.65%).

4.2. Assessing the performance of the spectral datasets in estimating post-fire ground cover fractions

Table 5 summarizes the results from the linear regression in the training set and their validation. Only models with a minimum threshold of $R^2_{adj.} \geqslant 0.50$ in any of the datasets are reported. Of the four absorption indices used for estimation, only the regression equations derived from BD data are shown due to the greater accuracy of the results obtained on this spectral dataset (difference in $R^2_{adj.}$ from 0.01 to 0.15). Accordingly, a total of 10 empirical models for the estimation of post-fire ground covers have been developed in this study with a number between 1 and 2 wavebands.

Stepwise regression on spectral data estimates the ground cover fraction of five post-fire components (GV, UBS, char, ash, and a combination of char/ash) to at least an accuracy of $R^2_{adj.} \geqslant 0.60$ in the best model. Estimation of components more related to moderate fire severity, like NPV and BS, has not achieved this accuracy level ($R^2_{adj.} < 0.40$), although the wavebands selected were always statistically significant at a ρ level of 0.05. Overall, $R^2_{adj.}$ values are largest for FDS and smallest for BD data.

GV is the ground cover best estimated, with $R^2_{adj.}$ values uniformly high (greater than 0.70) between all three forms of data in the training dataset, which can be attributed to the relative ease of sensing the canopy vegetation. Regarding the wavebands selected in the models, the well-documented contrast between red and NIR regions is the key to the predictive power of this ground cover: two wavebands (from the NIR plateau and red edge) on HCRF data and a single-band model on FDS (a band with one of the highest positive changes in reflectance) and BD data (one of the deepest bands of the 680-nm absorption feature). The $R^2_{adj.}$ between the estimated and observed GV fraction is slightly larger in the P_{EF} validation dataset (a mean increment of $R^2_{adj.}$ of 0.06, Table 5), which could be explained simply on the basis of n alone. Good results in the IZ_{WF} validation dataset ($R^2_{adj.}$ even higher except on the HCRF data) demonstrate the predictive power of these equations in a real application on samples from two different wildfires and different sensor. Although $R^2_{adj.}$ is a useful guide to the relative differences observed, the absolute error is of greatest interest for practical applications. These errors in GV estimation are very small and similar in magnitude (RMSE in the range 7.5–12.8). Considering the largest $R^2_{adj.}$ in the three datasets and the lowest RMSE in the IZ_{WF} validation dataset, with the closest 1:1 fit between observed and estimated GV fractions (Fig. 5. left column), FDS data can be considered the best predictor of this ground cover.

UBS, char, and ash (the latter two both as individual ground cover and as a combined product) are not well estimated from BD data (Table 5) due to the absence of absorption processes, as

Table 5
Summary of the SMLR models developed on the HCRF, FDS, and BD data. The accuracy of estimations is reported for training and validation datasets both in terms of the $R^2_{adj.}$ and the RMSE.

Post-fire ground cover	Regression model	Training dataset (P_{EF}, n = 217)		Validation dataset 1 (P_{EF}, n = 88)		Validation dataset 2 (IZ_{WF}, n = 51)	
		$R^2_{adj.}$	RMSE	$R^2_{adj.}$	RMSE	$R^2_{adj.}$	RMSE
HCRF dataset							
GV	$-2.006 + (2.743 \times HCRF\_B876) - (3.066 \times HCRF\_B695.12)$	0.724	8.809	0.787	7.828	0.658	12.755
UBS	$-7.717 + (4.357 \times HCRF\_B707.09) - (3.890 \times HCRF\_B400.24)$	0.506	15.618	0.676	14.625	0.389	28.887
Char	$31.624 - (1.151 \times HCRF\_B900.43)$	0.465	8.391	0.526	8.582	0.486	35.469
Ash	$7.631 + (11.635 \times HCRF\_B400.24) - (5.337 \times HCRF\_B576.74)$	0.786	6.520	0.771	7.241	0.368	32.697
Char/ash	$46.796 - (2.857 \times HCRF\_B900.43) + (5.816 \times HCRF\_B400.24)$	0.689	13.274	0.744	12.734	0.789	39.643
FDS dataset							
GV	$-0.575 + (132.298 \times FDS\_B710.51)$	0.745	8.471	0.779	8.048	0.896	7.475
UBS	$-0.090 + (981.892 \times FDS\_B434.98)$	0.607	13.925	0.730	13.466	0.708	18.034
Char	$25.245 - (734.278 \times FDS\_B759.32) + (154.946 \times FDS\_B677.99)$	0.620	7.077	0.606	7.889	0.297	36.137
Ash	$32.925 - (538.304 \times FDS\_B755.35) - (264.844 \times FDS\_776.83)$	0.598	8.929	0.569	9.655	0.112	29.535
Char/ash	$58.054 - (1366.975 \times FDS\_B756.49)$	0.685	13.308	0.705	13.390	0.711	33.119
BD dataset							
GV	$1.551 + (99.285 \times BD\_B705.95)$	0.705	9.118	0.777	8.045	0.898	11.663

Note: Only regression models with $R^2_{adj.} \geqslant 0.50$ in the training or validation datasets are shown in this table. All presented models are significant at $\rho < 0.05$. The base name of the selected wavebands refers to the spectral dataset used for estimation. Spectral band wavelengths are given in nm.
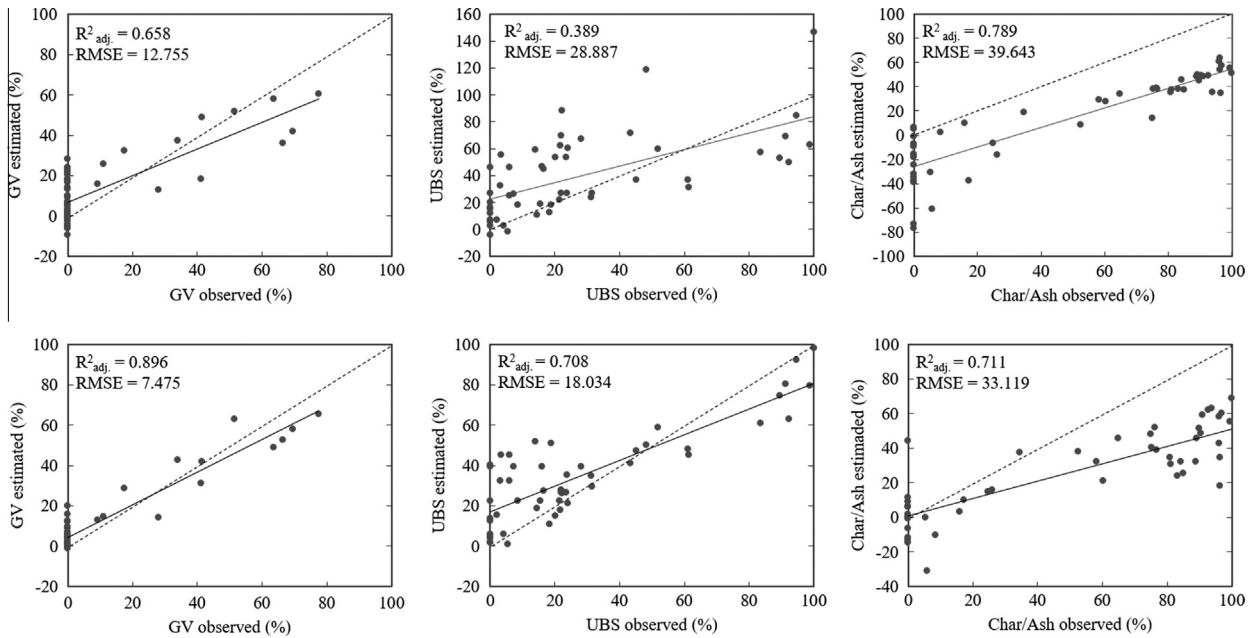
Fig. 5. Scatterplots of HCRF (above) and FDS (below) derived fractional ground cover versus the ground data in the IZ$_{WF}$ validation dataset. Linear regression lines are shown as solid lines and the 1:1 fit is shown as dotted lines.

described in Section 4.1. In UBS estimation, the different spectral behavior between the shortest bands of NIR and blue regions is highlighted in the HCRF model, and the reflectance change ratio in the first half of the same blue region is emphasized in the FDS model. Estimation achieves a moderate level of accuracy; about 50% and 60% of the variance in the data is explained by HCRF and FDS values, respectively, with very similar RMSE values. Validation on P$_{EF}$ data increases the accuracy in both spectral data (R^2_{adj} 0.17 higher in HCRF data and 0.12 higher in FDS data with a decrease of RMSE around 0.5–1 points). However, there is a marked difference in the results obtained on the IZ$_{WF}$ validation set. Whereas FDS data show an R^2_{adj} value of 0.71 and a RMSE slightly higher but in line with those of the P$_{EF}$ training and validation datasets, on HCRF data R^2_{adj} falls below 0.4 and RMSE stands at values near 30, two times higher (Table 5 and Fig. 5. middle column). This change can be explained by the previously mentioned (Section 4.1) differences in magnitude of the reflectance values of UBS between burned areas; differences that disappear in the derivative spectral data (Fig. 4).

Char and ash, as individual ground covers, can be estimated to a moderate to high accuracy level, as shown in the results of the training and validation dataset of P$_{EF}$ (Table 5). HCRF data seem a better predictor of ash fraction and conversely FDS data can be considered best suited for char fraction estimation. However, the performance of both spectral data is weaker when applying the empirical models to burned areas different from that on which they were developed (R^2_{adj} < 0.4 and RMSE in the range from 29.5% to 35.5%). Considering the wavebands selected, HCRF equations reflect the different spectral behavior in reflectance values of the two ash-related covers; the char model highlights a NIR waveband (longest wavelength of the spectral range), whereas the ash model focuses on two VIS wavebands (from blue and green regions). The spectral homogenization associated with first derivative transformation (both ground covers draw an almost flatted line, Fig. 4) hinders estimation of these ground covers in an individual approach. Thus, although the equations are different, the distance between the first wavebands of both models (responsible for 97% of the total variance explained by the models and both located around 750 nm) is just 4 nm.

As a char/ash combined ground cover, the results on HCRF and FDS data show a similar pattern in the P$_{EF}$ training and validation datasets (R^2_{adj} ∼ 0.7 and RMSE ∼ 13). Although in the practical application to other burned areas an underestimation of ground cover fraction is still observed (RMSE around 35), the fit between observed and estimated fractions improves to values above 0.7 (Table 5 and Fig. 5 right column). Considering the similarity of the statistics in these two equations, two factors explain the selection of FDS as the best-suited spectral data in estimating the char/ash combined ground cover: the development of a single-band prediction model and the noise-related problems that could be associated with a model, like the HCRF, based on two wavebands exactly placed on the endpoints of the spectral range.

5. Discussion

As has been reported in many studies (a.o. Lentile et al., 2009; Lewis et al., 2011, 2008; Riaño et al., 2002; Smith et al., 2007), quantification of post-fire ground cover can be used to estimate immediate effects and – more important for the management of burned areas – to predict ecosystem response with better results than those offered by the traditional spectral indices. Subpixel-based methods are the techniques most commonly used to derive abundance estimates of dominant ground components. If, by way of illustration, an R^2_{adj} threshold of 0.50 is selected, comparison of unmixed-derived estimates and observed fractions is below the threshold for the application of SMA or MTMF techniques (Lewis et al., 2007; Robichaud et al., 2007) and higher adjusted determination coefficients are only achieved when the multiple endmember SMA (MESMA) is used (Veraverbeke et al., 2012a). Unmixing thus becomes a complex technique that requires advanced data processing and careful selection of endmembers to fulfill the general criteria of spectral separability, spectral representativity, and spatial generality (Quintano et al., 2013).

The empirical approach adopted in this study is proposed as an alternative method capable of providing damage assessment in a quick and objective manner – something that is very important to enable effective and timely management responses. Empirical studies are not a common approach in the identification and

quantification of the components of burned areas. However, some examples can be found, with good results, as in the recent work of Pleniou and Koutsias (2013) where linear regression models were fitted to the spectral channels of Landsat and ASTER imagery to estimate the percentage of burned and non-burned areas at the pixel level with a high degree of accuracy ($R^2 > 0.80$). In the current study, developed at a detailed field scale, we sought to estimate the individual components of burned areas from hyperspectral data. Although tested in previous research for fire severity assessment (Kokaly et al., 2007; Parra, 2005), derivative and absorption data are for the first time used in the present study to derive fractional estimates of post-fire ground cover.

Empirical models developed explain the 60–75% of the variation of ground cover fractions. Percentage of unexplained variance can be attributed to a combination of factors: (i) possible deviations in the area sensed by both sensors – digital camera and field spectroradiometer – as they are not registering simultaneously; (ii) errors related to the assumption of a homogeneous circular FOV of the field spectroradiometers (Mac Arthur et al., 2007), which means that reflectance of some classified pixels could have not been registered and viceversa; (iii) confusion errors in the classification process; (iv) underestimation of reflectance in some samples due to shadows; (v) errors in the estimation when the observed variable is 0, because the absence of an specific ground cover do not clearly correspond to a single value of the dependent variable; and (vi) restriction to the 400–900 nm spectral range, that does not consider changes in reflectance associated to differences in water content or absorption bands specific of the senesced material or different soil characteristics.

Good results achieved in the estimation of GV and char/ash – those ground covers associated with extreme fire severity levels – are a general trend in the studies focusing on this approach to fire severity (Lewis et al., 2007; Veraverbeke et al., 2012a). In the same way, difficulties observed in the estimation of moderate severity levels are also a constant, not only in the quantification of NPV ground cover (Finley and Glenn, 2010) but also in other severity approaches based on indices like the CBI (De Santis and Chuvieco, 2007), the dNBR (Murphy et al., 2008), or the RdNBR (Miller et al., 2009). Specialized studies consider char and ash to be the post-fire ground covers with the greatest capacity to predict ecosystem response (Hudak et al., 2013); conversely, NPV fraction offers the worst performance (Hudak et al., 2007; Lentile et al., 2009). On this basis, the ability to quantify char/ash abundance is perhaps the most significant highlight of this research. Considering the spectral restriction to the VNIR region (400–900 nm), it is important to highlight that, although better results could be attained from VSWIR data, recent research has demonstrated the great potential of the NIR region in discriminating ground cover classes (Veraverbeke et al., 2014) or in estimating the percentage of burned areas at pixel level (Pleniou and Koutsias, 2013).

Three main issues should be considered for practical applications: the empirical approach, the time perspective, and hyperspectral data availability. The applicability of empirical models to different ecosystems or fire characteristics is always a difficult issue (Roy et al., 2013). In the current study, the models developed and validated in an experimental fire (P_{EF}) were applied to samples from two natural wildfires (I_{WF} and Z_{WF}). Though still focused on Mediterranean shrubland formations, these two areas represent a different scenario regarding (i) plant species composition, (ii) fire characteristics, and (iii) field spectra measurements (sensor with a different spectral interval, spectral resolution and SNR, as described in Section 3.1.3). The results achieved in the comparison of observed and HCRF-estimated fractions reveal the problems associated with the application of the models obtained from this spectral variable. Differences in reflectance values between burned areas, especially in UBS and ash ground cover, prevent general use

of these models. The reverse is the case in the equations developed on FDS data. Derivative spectra of post-fire ground cover proved broadly similar across the three burned areas (Section 4.1), giving good results in the comparison of observed and FDS-estimates and giving confidence in the applicability of the models. The main drawback observed in using FDS data is their inability to derive individual char and ash fractions, which could be especially important in helping to establish the threshold between moderate and high fire severity (Smith et al., 2010).

A second general limitation impacting this approach is that fire severity effects are mostly shortlived and therefore should be assessed in a short time window. Within days to months after fire activity, ash layers and vegetation remains are redistributed by wind, surface runoff, or by being incorporated into the soil (Balfour et al., 2014; Pereira et al., 2013; Pérez-Cabello et al., 2012). Fulfillment of this temporal requirement is even more difficult when spectral data availability is considered. On the one hand, proximal sensing is not a feasible approach for fire severity assessment in practical applications, because ground sampling procedure is time-consuming (as observed in Ibieca and Zuera study sites), labor intensive and restricted by the difficulties of access. On the other hand, hyperspectral images are currently acquired on demand by tasking spacecrafts (e.g. EO-1 Hyperion) or aircrafts (e.g. AVIRIS or CASI), which makes data acquisition expensive, logistically challenging and, consequently, not practical for directing post-fire mitigation efforts. In this context, two ways of improvement of hyperspectral data availability are identified. First, the upcoming spaceborne imaging spectrometry (IS) missions, such as EnMAP or HyspIRI, that, when fully operational, will allow consistent global mapping of fire severity. Second, the great evolution of Unmanned Aerial Vehicles (UAVs) (Colomina and Molina, 2014), an effective and flexible technology which satisfy the requirements of spatial, spectral, and temporal resolutions. Moreover, in the last decade, technological advances have made the development of micro-UAVs possible and affordable (Berni et al., 2009). Potential of this technology has been proved in fire science for monitoring, detecting and fighting forest fires (Martínez-de-Dios et al., 2007; Wing et al., 2014; Yuan et al., 2015), improving the cost effectiveness of such activities (Christensen, 2015). Recent relevant developments on hyperspectral sensors, with instruments like Hyperspec (Headwall Photonics, Inc.), capable of fitting the new class of lightweight UAVs, open the possibility to use this technology for fire severity assessment. Good results obtained in agricultural applications (Calderón et al., 2013; Zarco-Tejada et al., 2012, 2013) demonstrate the potential of these micro-hyperspectral imaging sensors on board of small UAV platforms to predict post-fire cover types.

6. Conclusions

The present study approaches to fire severity assessment through the quantification of post-fire ground covers. Specifically, empirical relationships were established between the HSRP-derived estimates of seven post-fire ground cover types and six sets of spectral data in three burned areas of Mediterranean shrubland.

A marked difference in the performance of the six datasets was observed. Taking a nominal $R^2_{adj.}$ threshold of 0.50, stepwise regression on absorption datasets (BD, BDR, NBDI, and BNA) estimates the abundance of only one ground cover (GV) to at least this accuracy; HCRF data increase this to four categories (GV, UBS, ash, and char/ash); and FDS data increase this further to five components (GV, UBS, char, ash, and char/ash). The best results were observed in the abundance estimation of GV, and char/ash ground covers. FDS data can be considered the best spectral variable for the following reasons: (i) the accuracy of estimations in the training dataset was always equal or better in this dataset; (ii) the results

of the application in the natural wildfires surpass those obtained with the other spectral data; (iii) the high predictive power attained with single-band models; and (iv) the absence of noise-related problems associated with the use of wavebands placed on the endpoints of the spectral range. Considering the FDS equations developed on this study, the near-infrared region has the highest discriminatory power for GV and ash-related ground covers and the blue region is especially suited for UBS estimation.

These empirically-based models may aid fire severity assessment by providing valuable information with which to predict ecosystem responses and, consequently, to guide strategies and restoration actions. Future work should explore validation in forested areas and other ecosystems, and analyze the improvement provided by the short-wave infrared spectral region. Additionally, an effort should be made to adapt the developed models to the spectral characteristics of different multi- and hyperspectral remote sensors, aiming for a more regional assessment of fire severity.

Acknowledgements

References

Arcenegui, V., Mataix-Solera, J., Guerrero, C., Zornoza, R., Mataix-Beneyto, J., García-Orenes, F., 2008. Immediate effects of wildfires on water repellency and aggregate stability in Mediterranean calcareous soils. Catena 74, 219–226.

Balfour, V.N., Doerr, S.H., Robichaud, P.R., 2014. The temporal evolution of wildfire ash and implications for post-fire infiltration. Int. J. Wildland Fire.

Berni, J.A.J., Zarco-Tejada, P.J., Suarez, L., Fereres, E., 2009. Thermal and narrowband multispectral remote sensing for vegetation monitoring from an unmanned aerial vehicle. IEEE Trans. Geosci. Remote Sens. 47, 722–738.

Bodí, M.B., Doerr, S.H., Cerdà, A., Mataix-Solera, J., 2012. Hydrological effects of a layer of vegetation ash on underlying wettable and water repellent soil. Geoderma 191, 14–23.

Bodí, M.B., Mataix-Solera, J., Doerr, S.H., Cerdà, A., 2011. The wettability of ash from burned vegetation and its relationship to Mediterranean plant species type, burn severity and total organic carbon content. Geoderma 160, 599–607.

Calderón, R., Navas-Cortés, J.A., Lucena, C., Zarco-Tejada, P.J., 2013. High-resolution airborne hyperspectral and thermal imagery for early detection of Verticillium wilt of olive using fluorescence, temperature and narrow-band spectral indices. Remote Sens. Environ. 139, 231–245.

Cerdà, A., Doerr, S.H., 2005. Influence of vegetation recovery on soil hydrology and erodibility following fire: an 11-year investigation. Int. J. Wildland Fire 14, 423–437.

Cerdà, A., Doerr, S.H., 2008. The effect of ash and needle cover on surface runoff and erosion in the immediate post-fire period. Catena 74, 256–263.

Colomina, I., Molina, P., 2014. Unmanned aerial systems for photogrammetry and remote sensing: a review. ISPRS J. Photogramm. Remote Sens. 92, 79–97.

Curran, P.J., Dungan, J.L., Peterson, D.L., 2001. Estimating the foliar biochemical concentration of leaves with reflectance spectrometry: testing the Kokaly and Clark methodologies. Remote Sens. Environ. 76, 349–359.

Christensen, B.R., 2015. Use of UAV or remotely piloted aircraft and forward-looking infrared in forest, rural and wildland fire management: evaluation using simple economic analysis. N. Z. J. Forest. Sci. 45.

Chuvieco, E., Giglio, L., Justice, C., 2008. Global characterization of fire activity: toward defining fire regimes from Earth observation data. Glob. Change Biol. 14, 1488–1502.

Dawson, T.P., Curran, P.J., 1998. Technical note: A new technique for interpolating the reflectance red edge position. Int. J. Remote Sens. 19, 2133–2139.

De Luís, M., Raventós, J., González-Hidalgo, J.C., 2005. Factors controlling seedling germination after fire in Mediterranean gorse shrublands. Implications for fire prescription. J. Environ. Manage. 76, 159–166.

De Luís, M., Raventós, J., González-Hidalgo, J.C., 2006. Post-fire vegetation succession in Mediterranean gorse shrublands. Acta Oecol. 30, 54–61.

De Santis, A., Chuvieco, E., 2007. Burn severity estimation from remotely sensed data: performance of simulation versus empirical models. Remote Sens. Environ. 108, 422–435.

De Santis, A., Chuvieco, E., 2009. GeoCBI: a modified version of the Composite Burn Index for the initial assessment of the short-term burn severity from remotely sensed data. Remote Sens. Environ. 113, 554–562.

Díaz-Delgado, R., Lloret, F., Pons, X., 2003. Influence of fire severity on plant regeneration by means of remote sensing imagery. Int. J. Remote Sens. 24, 1751–1763.

Doerr, S.H., Shakesby, R.A., Blake, W.H., Chafer, C.J., Humphreys, G.S., Wallbrink, P.J., 2006. Effects of differing wildfire severities on soil wettability and implications for hydrological response. J. Hydrol. 319, 295–311.

Edwards, A.C., Maier, S.W., Hutley, L.B., Williams, R.J., Russell-Smith, J., 2013. Spectral analysis of fire severity in north Australian tropical savannas. Remote Sens. Environ. 136, 56–65.

Epting, J., Verbyla, D., Sorbel, B., 2005. Evaluation of remotely sensed indices for assessing burn severity in interior Alaska using Landsat TM and ETM+. Remote Sens. Environ. 96, 328–339.

Finley, C.D., Glenn, N.F., 2010. Fire and vegetation type effects on soil hydrophobicity and infiltration in the sagebrush-steppe: II. Hyperspectral analysis. J. Arid Environ. 74, 660–666.

Gartzia, M., Alados, C.L., Pérez-Cabello, F., 2014. Assessment of the effects of biophysical and anthropogenic factors on woody plant encroachment in dense and sparse mountain grasslands based on remote sensing data. Prog. Phys. Geogr.

Hudak, A.T., Morgan, P., Bobbitt, M.J., Smith, A.M.S., Lewis, S.A., Lentile, L.B., Robichaud, P.R., Clark, J.T., McKinley, R.A., 2007. The relationship of multispectral satellite imagery to immediate fire effects. Fire Ecol. Spec. Issue 3, 64–90.

Hudak, A.T., Ottmar, R.D., Vihnanek, R.E., Brewer, N.W., Smith, A.M.S., Morgan, P., 2013. The relationship of post-fire white ash cover to surface fuel consumption. Int. J. Wildland Fire 22, 780–785.

Keeley, J.E., 2009. Fire intensity, fire severity and burn severity: a brief review and suggested usage. Int. J. Wildland Fire 18, 116–126.

Keeley, J.E., Brennan, T., Pfaff, A.H., 2008. Fire severity and ecosystem responses following crown fires in California shrublands. Ecol. Appl. 18, 1530–1546.

Keeley, J.E., Fotheringham, C.J., Baer-Keeley, M., 2005. Factors affecting plant diversity during post-fire recovery and succession of mediterranean-climate shrublands in California, USA. Divers. Distrib. 11, 525–537.

Key, C.H., Benson, N.C., 2006. Landscape assessment (LA). In: Lutes, D.C., Keane, R.E., Caratti, J.F., Key, C.H., Benson, N.C., Sutherland, S., Gangi, L.J. (Eds.), FIREMON: Fire Effects Monitoring and Inventory System. Gen. Tech. Rep. RMRS-GTR-164-CD. Department of Agriculture, Forest Service, Rocky Mountain Research Station, Fort Collins, p. 55.

Kokaly, R.F., Despain, D.G., Clark, R.N., Livo, K.E., 2003. Mapping vegetation in Yellowstone National Park using spectral feature analysis of AVIRIS data. Remote Sens. Environ. 84, 437–456.

Kokaly, R.F., Rockwell, B.W., Haire, S.L., King, T.V.V., 2007. Characterization of post-fire surface cover, soils, and burn severity at the Cerro Grande Fire, New Mexico, using hyperspectral and multispectral remote sensing. Remote Sens. Environ. 106, 305–325.

Komac, B., Kéfi, S., Escós, J., Alados, C.L., 2013. Modeling shrub encroachment in alpine grasslands under different environmental and management scenarios. J. Environ. Manage. 121, 160–169.

Lasanta, T., Errea, M.P., Vicente-Serrano, S.M., Arnáez, J., 2011. La diversidad de la cubierta vegetal en campos abandonados del Leza y Jubera (Sistema Ibérico, La Rioja) a partir del SIOSE. Zubía 23, 55–78.

Lentile, L.B., Holden, Z.A., Smith, A.M.S., Falkowski, M.J., Hudak, A.T., Morgan, P., Lewis, S.A., Gessler, P.E., Benson, N.C., 2006. Remote sensing techniques to assess active fire characteristics and post-fire effects. Int. J. Wildland Fire 15, 319–345.

Lentile, L.B., Smith, A.M.S., Hudak, A.T., Morgan, P., Bobbitt, M.J., Lewis, S.A., Robichaud, P.R., 2009. Remote sensing for prediction of 1-year post-fire ecosystem condition. Int. J. Wildland Fire 18, 594–608.

Lewis, S.A., Hudak, A.T., Ottmar, R.D., Robichaud, P.R., Lentile, L.B., Hood, S.M., Cronan, J.B., Morgan, P., 2011. Using hyperspectral imagery to estimate forest floor consumption from wildfire in boreal forests of Alaska, USA. Int. J. Wildland Fire 20, 255–271.

Lewis, S.A., Lentile, L.B., Hudak, A.T., Robichaud, P.R., Morgan, P., Bobbitt, M.J., 2007. Mapping ground cover using hyperspectral remote sensing after the 2003 Simi and Old wildfires in Southern California. J. Assoc. Fire Ecol. 3, 109–127.

Lewis, S.A., Robichaud, P.R., Frazier, B.E., Wu, J.Q., Laes, D.Y.M., 2008. Using hyperspectral imagery to predict post-wildfire soil water repellency. Geomorphology 95, 192–205.

López, M.J., Caselles, V., 1991. Mapping burns and natural reforestation using thematic Mapper data. Geocarto Int. 6, 31–37.

Mac Arthur, A.A., MacLellan, C., Malthus, T.J., 2007. Determining the FOV and directional response field spectroradiometers. Proceedings of the Fifth EARSeL Workshop on Imaging Spectroscopy: Innovation in Environmental Research. The European Association of Remote Sensing Laboratories, VITO, Ghent University and the Belgian Science Policy Office, Bruges, Belgium, pp. 1–8.

Martínez-de-Dios, J.R., Merino, L., Ollero, A., Ribeiro, L.M., Viegas, X., 2007. Multi-UAV experiments: application to forest fires. In: Ollero, A., Maza, I. (Eds.), Multiple Heterogeneous Unmanned Aerial Vehicles, STAR 37. Springer-Verlag, Berlin Heidelberg, pp. 207–228.

Mataix-Solera, J., Doerr, S.H., 2004. Hydrophobicity and aggregate stability in calcareous topsoils from fire-affected pine forests in southeastern Spain. Geoderma 118, 77–88.

Mataix-Solera, J., Gómez, I., Navarro-Pedreño, J., Guerrero, C., Moral, R., 2002. Soil organic matter and aggregates affected by wildfire in a *Pinus halepensis* forest in a Mediterranean environment. Int. J. Wildland Fire 11, 107–114.

Milton, E.J., Schaepman, M.E., Anderson, K., Kneubühler, M., Fox, N., 2009. Progress in field spectroscopy. Remote Sens. Environ. 113, S92–S109.

Miller, J.D., Knapp, E.E., Key, C.H., Skinner, C.N., Isbell, C.J., Creasy, R.M., Sherlock, J. W., 2009. Calibration and validation of the relative differenced Normalized Burn Ratio (RdNBR) to three measures of fire severity in the Sierra Nevada and Klamath Mountains, California, USA. Remote Sens. Environ. 113, 645–656.

Miller, J.D., Thode, A.E., 2007. Quantifying burn severity in a heterogeneous landscape with a relative version of the delta Normalized Burn Ratio (dNBR). Remote Sens. Environ. 109, 66–80.

Moody, J.A., Shakesby, R.A., Robichaud, P.R., Cannon, S.H., Martin, D.A., 2013. Current research issues related to post-wildfire runoff and erosion processes. Earth Sci. Rev. 122, 10–37.

Mouillot, F., Rambal, S., Joffre, R., 2002. Simulating climate change impacts on fire frequency and vegetation dynamics in a Mediterranean-type ecosystem. Glob. Change Biol. 8, 423–437.

Murphy, K.A., Reynolds, J.H., Koltun, J.M., 2008. Evaluating the ability of the differenced Normalized Burn Ratio (dNBR) to predict ecologically significant burn severity in Alaskan boreal forests. Int. J. Wildland Fire 17, 490–499.

Mutanga, O., Skidmore, A.K., Prins, H.H.T., 2004. Predicting in situ pasture quality in the Kruger National Park, South Africa, using continuum-removed absorption features. Remote Sens. Environ. 89, 393–408.

Neary, D.G., Klopatek, C.C., DeBano, L.F., Ffolliott, P.F., 1999. Fire effects on belowground sustainability: a review and synthesis. For. Ecol. Manage. 122, 51–71.

Noomen, M.F., Skidmore, A.K., van der Meer, F.D., Prins, H.H.T., 2006. Continuum removed band depth analysis for detecting the effects of natural gas, methane and ethane on maize reflectance. Remote Sens. Environ. 105, 262–270.

Pannkuk, C.D., Robichaud, P.R., 2003. Effectiveness of needle cast at reducing erosion after forest fires. Water Resour. Res. 39.

Parra, A., 2005. Estimación de niveles de severidad del fuego a partir de datos hiperespectrales EO-1 Hyperion. Departamento de Geografía. Universidad de Alcalá, Alcalá de Henares, p. 254.

Pausas, J.G., Llovet, J., Rodrigo, A., Vallejo, R., 2008. Are wildfires a disaster in the Mediterranean basin? – A review. Int. J. Wildland Fire 17, 713–723.

Pereira, P., Cerdà, A., Úbeda, X., Mataix-Solera, J., Martin, D., Jordán, A., Burguet, M., 2013. Spatial models for monitoring the spatio-temporal evolution of ashes after fire – a case study of a burnt grassland in Lithuania. Solid Earth 4, 153–165.

Pérez-Cabello, F., Cerdà, A., de la Riva, J., Echeverría, M.T., García-Martín, A., Ibarra, P., Lasanta, T., Montorio, R., Palacios, V., 2012. Micro-scale post-fire surface cover changes monitored using high spatial resolution photography in a semiarid environment: a useful tool in the study of post-fire soil erosion processes. J. Arid Environ. 76, 88–96.

Pérez-Cabello, F., de la Riva Fernández, J., Montorio Llovería, R., García-Martín, A., 2006. Mapping erosion-sensitive areas after wildfires using fieldwork, remote sensing, and geographic information systems techniques on a regional scale. J. Geophys. Res. 111, G04S10.

Picotte, J.J., Robertson, K.M., 2011. Validation of remote sensing of burn severity in south-eastern US ecosystems. Int. J. Wildland Fire 20, 453–464.

Pleniou, M., Koutsias, N., 2013. Sensitivity of spectral reflectance values to different burn and vegetation ratios: a multi-scale approach applied in a fire affected area. ISPRS J. Photogramm. Remote Sens. 79, 199–210.

Quintano, C., Fernández-Manso, A., Roberts, D.A., 2013. Multiple Endmember Spectral Mixture Analysis (MESMA) to map burn severity levels from Landsat images in Mediterranean countries. Remote Sens. Environ. 136, 76–88.

Riaño, D., Chuvieco, E., Ustin, S., Zomer, R., Dennison, P., Roberts, D., Salas, J., 2002. Assessment of vegetation regeneration after fire through multitemporal analysis of AVIRIS images in the Santa Monica Mountains. Remote Sens. Environ. 79, 60–71.

Robichaud, P.R., Lewis, S.A., Laes, D.Y.M., Hudak, A.T., Kokaly, R.F., Zamudio, J.A., 2007. Postfire soil burn severity mapping with hyperspectral image unmixing. Remote Sens. Environ. 108, 467–480.

Rodrigo, A., Retana, J., Picó, F.X., 2004. Direct regeneration is not the only response of mediterranean forests to large fires. Ecology 85, 716–729.

Roy, D.P., Boschetti, L., Smith, A.M., 2013. Satellite remote sensing of fires. In: Belcher, C.M. (Ed.), Fire Phenomena and the Earth System: An Interdisciplinary Guide to Fire Science. John wiley & Sons, pp. 77–93.

Roy, D.P., Boschetti, L., Trigg, S.N., 2006. Remote sensing of fire severity: assessing the performance of the normalized burn ratio. IEEE Geosci. Remote Sens. Lett. 3, 112–116.

Savitzky, A., Golay, M.J.E., 1964. Smoothing and differentiation of data by simplified least squares procedures. Anal. Chem. 36, 1627–1639.

Schaepman-Strub, G., Schaepman, M.E., Painter, T.H., Dangel, S., Martonchik, J.V., 2006. Reflectance quantities in optical remote sensing – definitions and case studies. Remote Sens. Environ. 103, 27–42.

Shakesby, R.A., Doerr, S.H., 2006. Wildfire as a hydrological and geomorphological agent. Earth Sci. Rev. 74, 269–307.

Smith, A.M.S., Drake, N.A., Wooster, M.J., Hudak, A.T., Holden, Z.A., Gibbons, C.J., 2007. Production of Landsat ETM+ reference imagery of burned areas within Southern African savannahs: comparison of methods and application to MODIS. Int. J. Remote Sens. 28, 2753–2775.

Smith, A.M.S., Eitel, J.U.H., Hudak, A.T., 2010. Spectral analysis of charcoal on soils: implications for wildland fire severity mapping methods. Int. J. Wildland Fire 19, 976–983.

Smith, A.M.S., Wooster, M.J., Drake, N.A., Dipotso, F.M., Falkowski, M.J., Hudak, A.T., 2005. Testing the potential of multi-spectral remote sensing for retrospectively estimating fire severity in African Savannahs. Remote Sens. Environ. 97, 92–115.

Steinier, J., Termonia, Y., Deltour, J., 1972. Comments on Smoothing and differentiation of data by simplified least square procedure. Anal. Chem. 44, 1906–1909.

Tanase, M., de la Riva, J., Pérez-Cabello, F., 2011. Estimating burn severity at the regional level using optically based indices. Can. J. For. Res. 41, 863–872.

Tedim, F., Remelgado, R., Borges, C., Carvalho, S., Martins, J., 2013. Exploring the occurrence of mega-fires in Portugal. For. Ecol. Manage. 294, 86–96.

van Wagtendonk, J.W., Root, R.R., Key, C.H., 2004. Comparison of AVIRIS and Landsat ETM+ detection capabilities for burn severity. Remote Sens. Environ. 92, 397–408.

Veraverbeke, S., Hook, S.J., Harris, S., 2012a. Synergy of VSWIR (0.4–2.5 μm) and MTIR (3.5–12.5 μm) data for post-fire assessments. Remote Sens. Environ. 124, 771–779.

Veraverbeke, S., Lhermitte, S., Verstraeten, W.W., Goossens, R., 2010. The temporal dimension of differenced Normalized Burn Ratio (dNBR) fire/burn severity studies: the case of the large 2007 Peloponnese wildfires in Greece. Remote Sens. Environ. 114, 2548–2563.

Veraverbeke, S., Somers, B., Gitas, I., Katagis, T., Polychronaki, A., Goossens, R., 2012b. Spectral mixture analysis to assess post-fire vegetation regeneration using Landsat Thematic Mapper imagery: accounting for soil brightness variation. Int. J. Appl. Earth Observ. Geoinf. 14, 1–11.

Veraverbeke, S., Stavros, E.N., Hook, S.J., 2014. Assessing fire severity using imaging spectroscopy data from the Airborne Visible/Infrared Imaging Spectrometer (AVIRIS) and comparison with multispectral capabilities. Remote Sens. Environ. 154, 153–163.

Vicente-Serrano, S.M., Pérez-Cabello, F., Lasanta, T., 2011. Pinus halepensis regeneration after a wildfire in a semiarid environment: assessment using multitemporal Landsat images. Int. J. Wildland Fire 20, 195–208.

Wing, M., Burnett, J.D., Sessions, J., 2014. Remote sensing and unmanned aerial system technology for monitoring and quantifying forest fire impacts. Int. J. Remote Sens. Appl. 4, 18–35.

Woods, S.W., Balfour, V.N., 2008. The effect of ash on runoff and erosion after a severe forest wildfire, Montana, USA. Int. J. Wildland Fire 17, 535–548.

Yuan, C., Zhang, Y., Liu, Z., 2015. A survey on technologies for automatic forest fire monitoring, detection, and fighting using unmanned aerial vehicles and remote sensing techniques. Can. J. For. Res. 45, 783–792.

Zarco-Tejada, P.J., González-Dugo, V., Berni, J.A.J., 2012. Fluorescence, temperature and narrow-band indices acquired from a UAV platform for water stress detection using a micro-hyperspectral imager and a thermal camera. Remote Sens. Environ. 117, 322–337.

Zarco-Tejada, P.J., Guillén-Climent, M.L., Hernández-Clemente, R., Catalina, A., González, M.R., Martín, P., 2013. Estimating leaf carotenoid content in vineyards using high resolution hyperspectral imagery acquired from an unmanned aerial vehicle (UAV). Agric. For. Meteorol. 171–172, 281–294.

Zhu, Z., Key, C.H., Ohlen, D., Benson, N.C., 2006. Evaluate sensitivities of burn severity mapping algorithms for different ecosystems and fire histories in the United States. Final Report to the Joint Fire Science Program: Project JFSP 01-1-4-12, Sioux Falls, p. 35.